Should the oxygen source be considered in the initiation of KCl-induced high-temperature corrosion?

Corrosion Science 183 (2021) 109332

Contents lists available at ScienceDirect

Corrosion Science

journal homepage: www.elsevier.com/locate/corsci

Should the oxygen source be considered in the initiation of KCl-induced high-temperature corrosion?

Juho Lehmusto [a,*], Mohammad Sattari [b], Mats Halvarsson [b], Leena Hupa [a]

[a] Combustion and Materials Chemistry, Johan Gadolin Process Chemistry Centre, Abo Akademi University, FI-20500, Turku, Finland
[b] Microstructure Physics, Department of Physics, Chalmers University of Technology, SE-412 96, Göteborg, Sweden

ARTICLE INFO

Keywords:
A: Alloy
A: Stainless steel
B: SEM
B: SIMS
B: TEM
B: XPS
C: High temperature corrosion

ABSTRACT

The role of two oxygen sources, oxygen and water vapor, in the initiation of KCl-induced high-temperature corrosion was addressed by studying two high-alloyed commercial materials at 550 °C. The differentiation between the two oxygen sources was implemented with ^{18}O-enriched water and $^{16}O_2$.

Based on the results, the solid-solid reaction between KCl(s) and the protective oxide on the alloy surface appeared to be more responsible for corrosion than the gas-solid reaction between KCl(g) and the protective oxide. Water was more involved in the abovementioned reactions than O_2: ^{18}O was the main oxygen isotope found in the formed surface oxides and intermediates.

1. Introduction

The strive for more sustainably produced power keeps the interest in renewable and waste-derived fuels growing. However, before becoming a realistic alternative, the steam temperatures in biomass- and waste-fired power plants have to be sufficiently high for an acceptable power production efficiency. There are specific characteristics of the aforementioned solid fuels, which make the raise of operation temperatures challenging. The feedstocks tend to contain moisture and various aggressive species, which, when released during combustion, dramatically increase the risk of high-temperature corrosion of heat-transfer components. The corrosion is caused mainly by deposits, formed when partly-molten and sticky fly ash particles adhere to surfaces with temperatures lower than that of the flue gas. The chemical composition of the feedstock may vary greatly, but potassium and chlorine are abundantly present in biomass and waste-derived fuels and therefore, generally considered to be among the most relevant species in high-temperature corrosion [1,2]. These two elements are usually found as potassium chloride (KCl) in the deposits.

The moisture content of the feedstock is one of the key factors affecting the boiler efficiency and it varies greatly between feedstocks, typically being 40−50 wt.% for biomass [3]. Combustion of moist solid fuel results in humid flue gas conditions during the combustion process. As a consequence, water vapor is available besides air as an oxygen source for the high-temperature corrosion reactions. For materials and plant designers, it would be valuable to know, how humidity affects high-temperature corrosion and should the moisture content of the fuel be taken into account because of this. KCl-induced corrosion under humid conditions has been studied both in laboratory-scale experiments e.g. [4–6] and in full-scale measurements e.g. [7–9]. Although separate details are still elusive, consensus prevails regarding the general progression of the reaction. In the presence of humidity, the degradation of the protective chromium-rich surface oxide commences with potassium chromate (K_2CrO_4) formation, which depletes chromium from the oxide, converting it into a porous iron-rich oxide, which offers little protection (Eq. 1) [10]. The porosity of the iron-rich oxide allows chlorine to migrate into the bulk material, and corrosion continues through metal chloride formation and further oxidation.

$$2(Cr_{1-x}Fe_x)_2O_3(s) + 8KCl(s) + 3O_2(g) + 4H_2O(g) = 2xFe_2O_3(s) + 4(1-x)K_2CrO_4(s) + 8HCl(g) \quad (1)$$

Unfortunately, even though the synergistic impact of air and water vapor on high-temperature corrosion can be designated, it is difficult to pinpoint the separate roles of these two oxygen sources. For this task, the utilization of isotope-enriched reagents may be of great advantage. The stable ^{18}O isotope has proven to be versatile as a tracer and has been applied to studies addressing the influence of oxygen on the mechanism of oxide layer formation on stainless steel [11]; the formation of aluminum oxide scales on high-temperature alloys [12]; the movement of gasses at solid oxide fuel cell interfaces [13]; silicon oxidation in

* Corresponding author.
E-mail address: juho.lehmusto@abo.fi (J. Lehmusto).

https://doi.org/10.1016/j.corsci.2021.109332
Received 30 October 2020; Received in revised form 16 February 2021; Accepted 17 February 2021
Available online 19 February 2021

Table 1
The chemical composition of the studied alloys in atomic percent.

Alloy	Fe	Cr	Ni	Mo	Al	Others
Sanicro 28	36.3	29.6	28.7	1.6	0.2	Mn: 1.7; Cu: 1.2; Si: 0.6
Alloy 625	4.2	24.4	63.0	5.3	0.5	Nb: 2.0; Ti: 0.5

semiconductors [14], and catalysts in the petrochemical industry [15]. The simultaneous use of stable oxygen isotopes as $^{16}O_2$ and $H_2^{18}O$ in high-temperature research has been scarcer. They have been applied to some extent to study oxidation kinetics [16,17] and oxide scale growth mechanism [18]. However, these experiments have been carried out in two stages, over long exposure times, or in the absence of KCl. Besides, the characterization of the samples in the studies involving KCl has been performed from the sample surface instead of cross-sections [19].

For an even more precise understanding regarding the importance of oxygen sources in the KCl-induced high-temperature corrosion, an elaborated study utilizing modern characterization tools would be beneficial. Moreover, the first stages of the corrosion reaction should be addressed to shed more light on the initiation of high-temperature corrosion and to connect the initiation with the subsequent reaction stages. To contribute to this, the goal of this study is to identify the distribution of oxygen in an oxide formed in the presence of potassium chloride. The focus is on the significance of the oxygen source – regarding the oxidation of the alloy, does it matter, whether oxygen originates from air or water vapor?

2. Experimental

Quadratic sample pieces (2cm × 2cm, thickness 0.5 cm) of high-alloyed materials Sanicro 28 and Alloy 625 were polished with SiC papers up to a grit of 1000. The samples were then cleaned with acetone and washed with ethanol in an ultrasonic bath. The alloy compositions, measured by Scanning Electron Microscopy/Energy Dispersive X-ray analysis (SEM-EDX), are given in Table 1. The high-temperature exposures were carried out in a quartz reactor located inside of a horizontal tube furnace. The target temperature was 550 °C, to which the furnace was heated with a heating rate of 8 °C min^{-1}. The samples were kept at the target temperature for 270 min in synthetic air (20 vol.% O_2, 80 vol. % N_2) under humid conditions. The humidity level of 10 vol% was created by introducing ^{18}O-enriched water (^{18}O content > 98 %, GMP quality, Rotem Industries Ltd.) into a pre-heater, where it vaporized and mixed with the synthetic air before entering the reactor. The total gas flow rate was kept at 0.2 dm^3 min^{-1} (0.13 m/min). Both heating and cooling of the furnace were carried out in an inert N_2 atmosphere to avoid reactions outside the isothermal stage. Potassium chloride (PA-grade, Merck) was dried, ground, sieved into a fraction of 50−100 μm, and pressed into pellets with a diameter of 8 mm and a thickness of 2 mm. Before the experiments, the pellets were stored in a desiccator and positioned with tweezers onto the sample surface just before the high-temperature exposure. After the exposure, the pellets were removed prior to the surface characterization. Sanicro 28 samples with no KCl were used as references; one was positioned on the windward side and the other on the leeward side of all samples with the KCl pellets (Fig. 1).

The morphology and the chemical composition of the oxidized surfaces were examined by SEM-EDX. The microscope (LEO Gemini 1530 with a NORAN Vantage X-ray analyzing system manufactured by Thermo Fisher Scientific) was operated in secondary and backscattering electron modes at an accelerating voltage of 20 kV for the EDX analyses and imaging with an aperture size of either 30 or 60 μm and a beam current of 1 nA. For distinguishing the different chemical states of certain elements at the sample surfaces, X-ray photoelectron spectroscopy (XPS) measurements were performed by using a Physical Electronics Quantum 2000 instrument combined with a monochromatic Al Kα X-ray excitation, operated at 46.7 W, and charge compensation by using low-energy electrons and Ar^+ ions. The diameter of the analysis spot was 200 μm.

The oxygen isotope distribution at the sample surfaces was analyzed employing ToF-SIMS (PHI TRIFT II, ULVACPHI Inc.). The measurements were performed by using 25 kV Ga^+ ions and an analysis spot with a diameter of one micrometer and an analysis depth of around five nanometers. The gallium ions sputter atoms and/or atom groups from the sample surface, after which the ablated species can be distinguished and identified by their mass-to-charge ratios.

Cross-sectional thin lamellae from the oxidized samples were prepared using the *in situ* lift-out technique in an FEI Versa 3D focused ion beam/scanning electron microscope (FIB/SEM). The lamellae were thinned down to approximately 100 nm thickness. In order to protect the surface from ion beam damage, two layers of Pt was deposited on the sample surface using first the electron beam followed by the ion beam of the FIB/SEM before ion milling.

A CAMECA NanoSIMS 50 L secondary ion mass spectrometer (CAMECA, Gennevilliers, France) was used to collect $^{16}O^-$, $^{16}OH^-$, $^{18}O^-$, $^{35}Cl^-$ images by rastering the FIB slice samples with a 0.6–1 pA and 16 keV Cs^+ primary ion beam. The spatial resolution of these images is between 100−160 nm (16 %–84 % step profile). The mass spectrometer collecting the secondary ions was set up with an entrance slit of 25 μm width, an aperture slit of 350 μm width, and a wide-open energy slit. The secondary ion intensities were measured with an electron multiplier in counting mode. The deadtime of each electron multiplier was set at 44 ns.

After NanoSIMS analyses, scanning transmission electron microscopy (STEM) imaging and EDX analysis were carried out on the samples in an FEI Titan 80–300 microscope (operated at 300 kV). High-angle annular dark-field (HAADF) imaging mode was used to image the samples and to give an atomic number contrast. The chemical analysis was performed by EDX using an Oxford Instruments INCA X-sight detector.

Fig. 1. A schematic drawing of the exposure setup, showing the two sample pieces *without* and the four sample pieces *with* the KCl pellets.

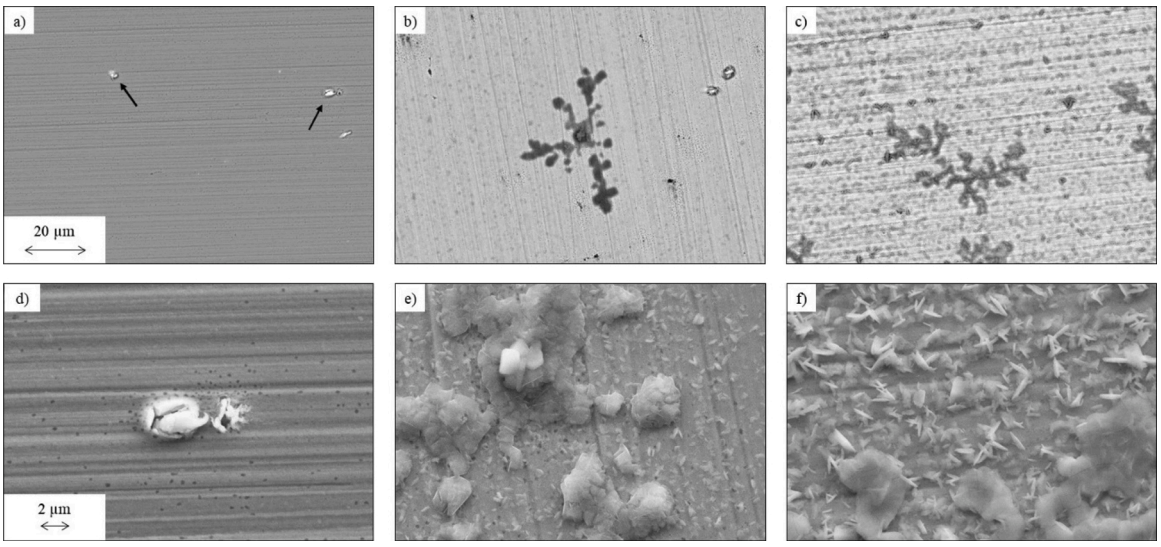

Fig. 2. Surface SEM images of the alloy Sanicro 28 samples exposed at 550 °C for 270 min. Images were taken from the sample positioned on the windward side of KCl (a,d); from the surface outside of the KCl pellet (b,e); and from the sample positioned on the leeward side of KCl (c,f).

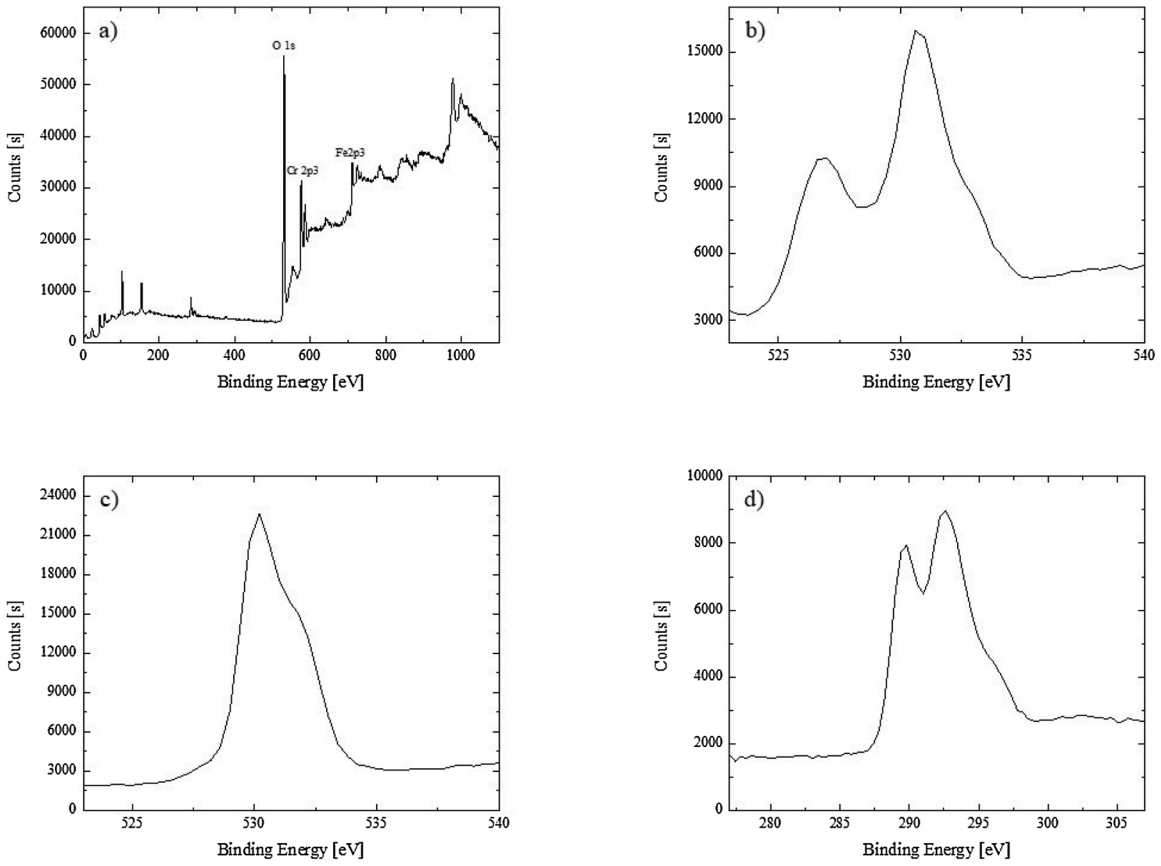

Fig. 3. XPS surface spectrum of the reference sample of Sanicro 28, located at the windward side of the KCl-containing samples (a). Only the main peaks are appointed.; XPS oxygen signal recorded at the edge of the KCl pellet (b); XPS oxygen signal recorded outside of the KCl pellet (c); and XPS potassium signal recorded at the edge of the KCl pellet (d).

3. Results and discussion

3.1. Surface analyses

The reference sample of Sanicro 28 located on the windward side of the KCl-containing samples generally oxidized homogeneously, forming a thin oxide (Fig. 2a). The XPS surface spectra (Fig. 3a) identified oxygen, chromium, and iron, suggesting the formation of chromium (Cr_2O_3) and $(Fe,Cr)_3O_4$ spinel oxides [20,21]. The alloy surface was punctured by sporadic structures consisting of cerium and oxygen, most likely as cerium oxide (CeO_2), which forms before the chromium and iron oxides [22]. Interestingly, the reference sample located on the leeward side had

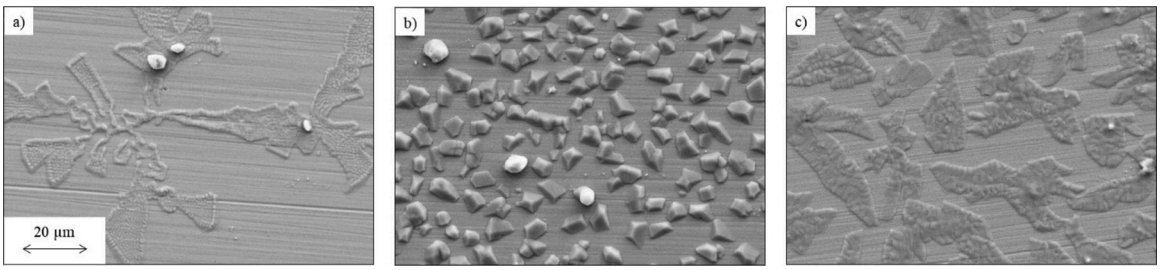

Fig. 4. Surface SEM images of the Alloy 625 sample exposed to KCl at 550 °C for 270 min; outside of the KCl pellet (a); at the edge of the KCl pellet (b); and underneath the KCl pellet (c).

an entirely different surface morphology with separate leaf-like features (Fig. 2c) and a generally rougher surface with a distinct microstructure (Fig. 2f). The leaf-like structure contained potassium but no chlorine, indicating strongly K_2CrO_4 formation as a result of the gas-phase diffusion of KCl [23,24].

Regarding the sample with the KCl pellet, potassium chromate formed in the solid-solid reaction between the surface oxide and the KCl pellet as well as in the solid-gas reaction between the surface oxide and vaporized KCl. The number of K_2CrO_4 particles was higher below and at the edge of the KCl pellet. Outside the pellet, the appearance of K_2CrO_4 resembled the leaf-like feature found on the reference sample (Fig. 2b, c). The higher amount of K_2CrO_4 in the vicinity of the KCl pellet was also detected in the XPS surface spectra, in which a split oxygen peak was recorded at the edge and underneath the KCl pellet (Fig. 3b), whereas the oxygen signal recorded from outside the KCl pellet only had one peak (Fig. 3c). The XPS signal for oxygen in Cr_2O_3 has one peak with the binding energy of approximately 529 eV [25], so the split oxygen signal indicates the presence of another oxygen-containing species. With the fact that no chlorine was detected from the surface and that the binding energy of the recorded potassium signal peaks (289.7 and 292.5 eV in Fig. 3d) agreed well with the previously reported one for high-purity K_2CrO_4 [25], it is suggested that K_2CrO_4 formed in a reaction can also be identified with XPS. At least for the short exposure time (270 min) used in the study, based on the amount of formed K_2CrO_4, the solid-solid reaction appears to be more responsible for alloy's chromium depletion than the gas-solid reaction. No increase in the number of K_2CrO_4

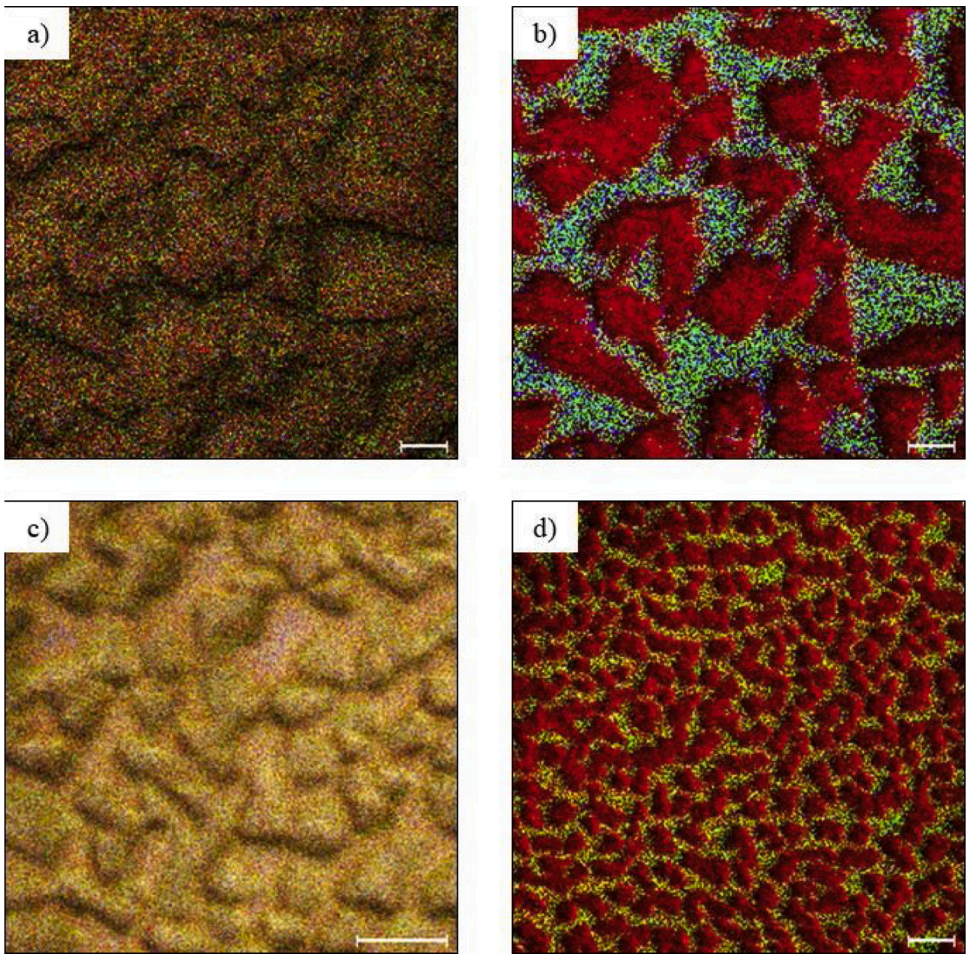

Fig. 5. Surface ToF-SIMS images of the alloys 625 (a,b) and Sanicro 28 (c,d) exposed to KCl at 550 °C for 270 min in synthetic air with $H_2^{18}O$. a) and c): ^{16}O is red, ^{18}O is green, Cl is blue; b) and d): Fe is green, K is red, Ni is blue. The scale bar equals 10 µm. Analyses were taken from underneath the KCl pellet. (For interpretation of the references to colour in this figure legend, the reader is referred to the web version of this article.)

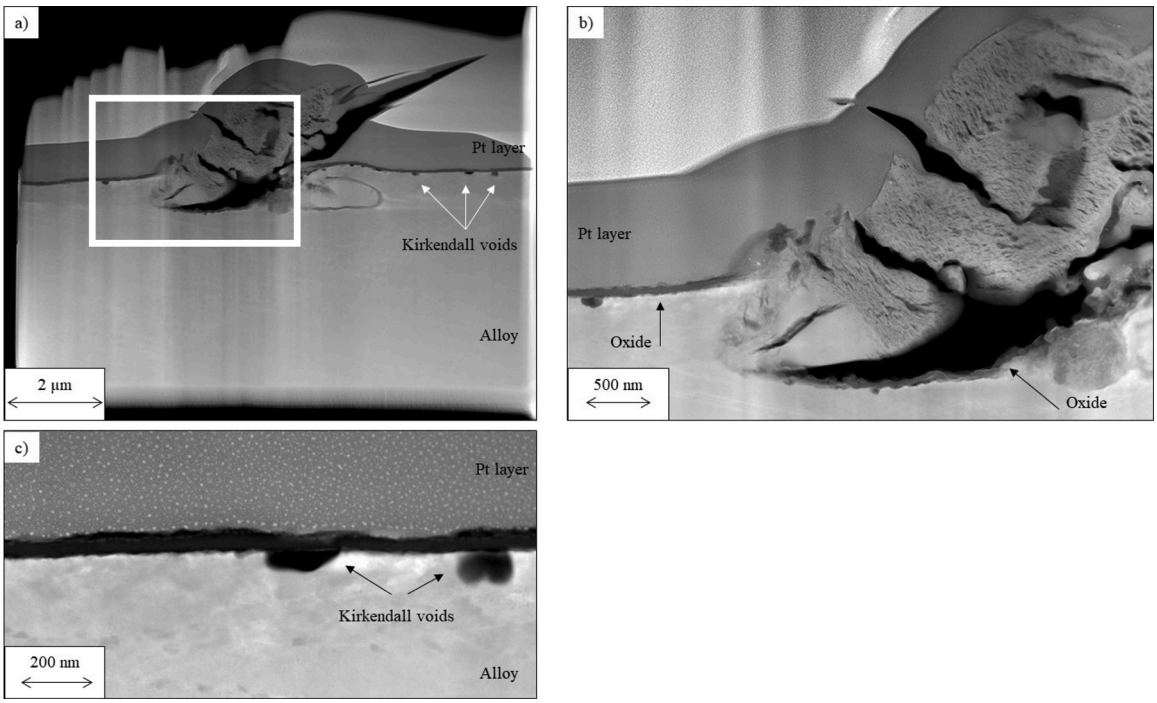

Fig. 6. An STEM HAADF image of an oxidized cerium inclusion in the Sanicro 28 reference sample (a). The area inside the white rectangular is magnified in image (b) and the Kirkendall voids in image (c).

particles was observed in the vicinity of the oxidized cerium inclusions, so these inclusions did not appear to function as seed points for K_2CrO_4 formation.

K_2CrO_4 particles were identified also on the Alloy 625 sample surface (Fig. 4). The number of K_2CrO_4 particles was highest underneath and at the edge of the KCl pellet, but the morphology of the particles differed somewhat, depending on the location. Underneath the pellet, the particles resembled thin sheets, whereas pyramid-shaped particles were found at the edge of the KCl pellet (Fig. 4b,c). The cause of the different morphologies could not be determined, but it might depend on the local oxygen partial pressure, which is known to affect crystal size and morphology through the defect and oxygen vacancy concentrations [26, 27]. Outside the KCl pellet, K_2CrO_4 was identified only in a few locations (Fig. 4a). The morphology was similar to that found outside the KCl pellet on Sanicro 28 and the Sanicro 28 reference sample on the leeward side of the KCl pellets (Fig. 2b,c). The XPS results (not shown here) were equivalent to the ones measured for Sanicro 28, confirming the formation of K_2CrO_4 in the reaction between Alloy 625 and KCl. In addition to K_2CrO_4 formation, several niobium oxide particles were identified protruding the alloy surface. Similar behavior has been reported at 500 °C with an Nb-stabilized alloy, where Nb_2O_5 particles formed rapidly during the exposure [21]. Similarly to the CeO_2 particles in the case of Sanicro 28, it could not be verified that Nb_2O_5 particles would function as seed points for enhanced K_2CrO_4 formation.

The presence of potassium-rich particles with no chlorine at the surface of both studied alloys was verified also with ToF-SIMS (Fig. 5). The oxygen isotopes were not as clearly distinguishable as in previous studies, where ^{16}O from the air was located in larger quantities in K_2CrO_4 particles, whereas ^{18}O from water vapor enriched onto the alloy surface [19]. The more even distribution of oxygen isotopes in the current study could originate from the longer exposure time, which allows the surface oxide to grow thicker and more time for the species to

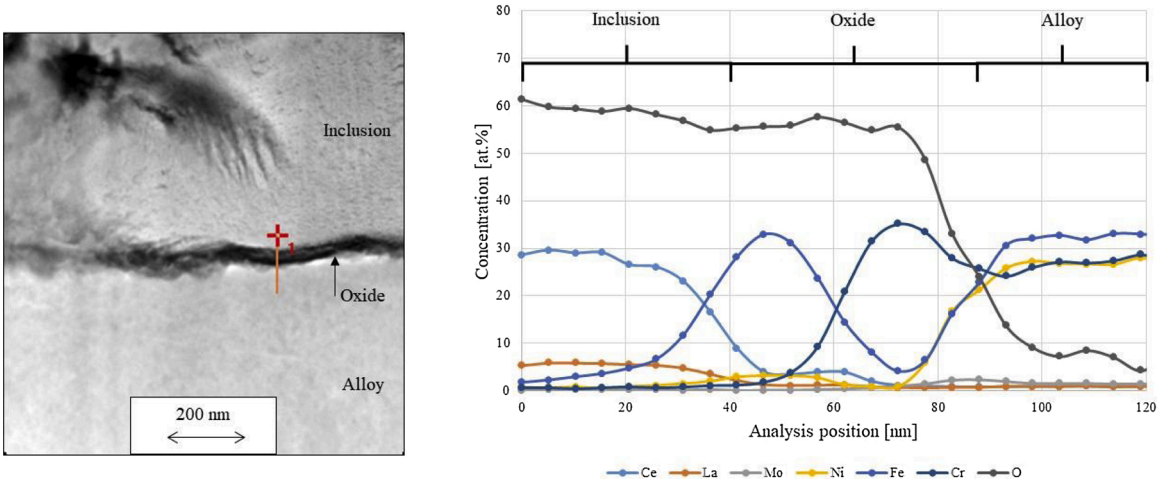

Fig. 7. An EDX line scan from the (Ce,La) inclusion over the thin oxide beneath. The red cross marks the starting point of the line scan. (For interpretation of the references to colour in this figure legend, the reader is referred to the web version of this article.)

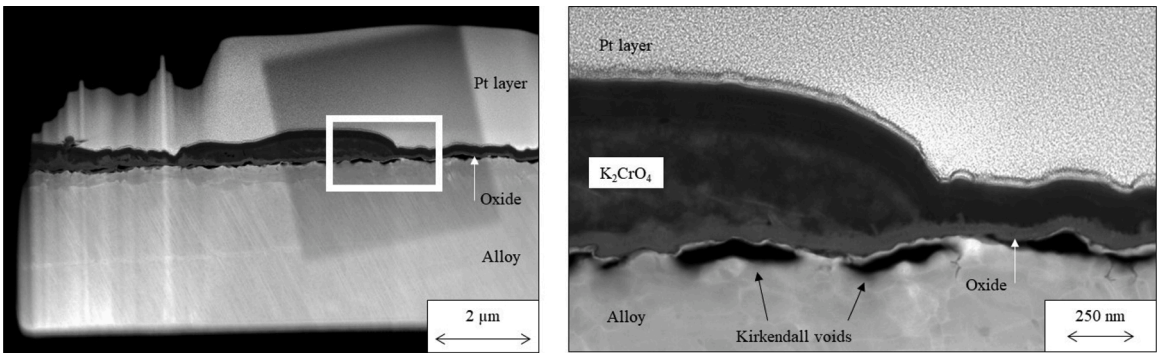

Fig. 8. STEM HAADF images of a K_2CrO_4 particle on the Sanicro 28 sample with KCl. The area inside the white rectangular is magnified on the right-hand image.

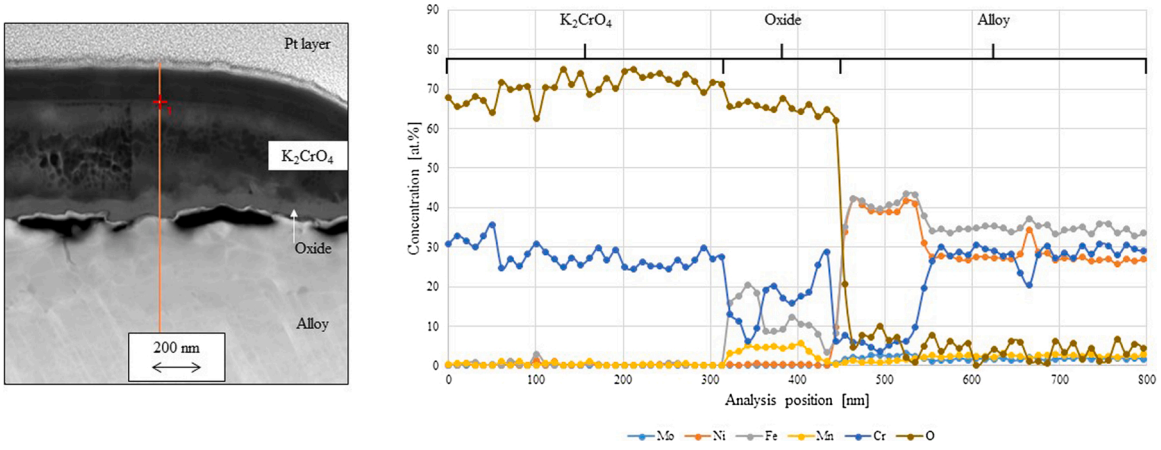

Fig. 9. An EDX line scan (position indicated in the left figure) through a K_2CrO_4 particle, the thin oxide scale, and the metal in the Sanicro 28 sample. The red cross marks the starting point of the line scan. (For interpretation of the references to colour in this figure legend, the reader is referred to the web version of this article.)

migrate into the formed oxide. Nevertheless, based on the ToF-SIMS maps (not shown here), it appears that in analyses further from the KCl pellet or from the reference sample located on the leeward side of the KCl, higher amounts of ^{18}O were recorded than from below the KCl pellet. This agrees well with water molecules usually being the preferred reactant instead of the oxygen molecules due to the higher adsorption and dissociation rates of water molecules compared to molecular oxygen [28,29].

3.2. Cross-sectional analyses

3.2.1. FIB-TEM

The thin cross-sectional FIB-TEM lamella of the reference Sanicro 28 sample located on the windward side of the KCl pellets contained an oxidized inclusion protruding the alloy surface (Fig. 6). Apart from the oxidized inclusion consisting of cerium and lanthanum oxide (confirmed by EDX), a thin oxide of around 50 nm covered the sample surface, also underneath the partly-detached inclusion. The oxide had a duplex structure with an iron-containing outer $(Fe,Cr)_3O_4$ spinel and a

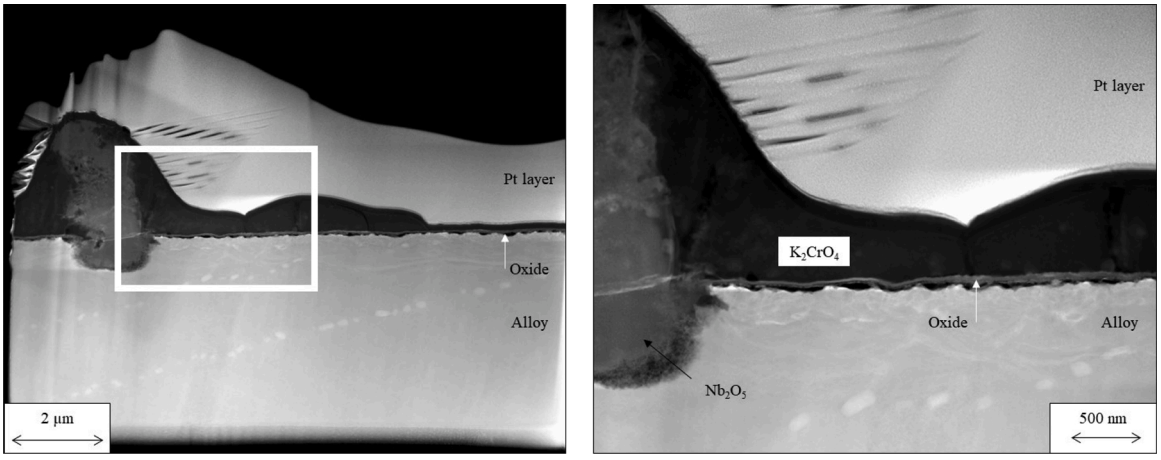

Fig. 10. STEM HAADF images of an oxidized niobium inclusion together with a K_2CrO_4 particle on the Alloy 625 sample with KCl. The area inside the white rectangular is magnified in the right-hand image.

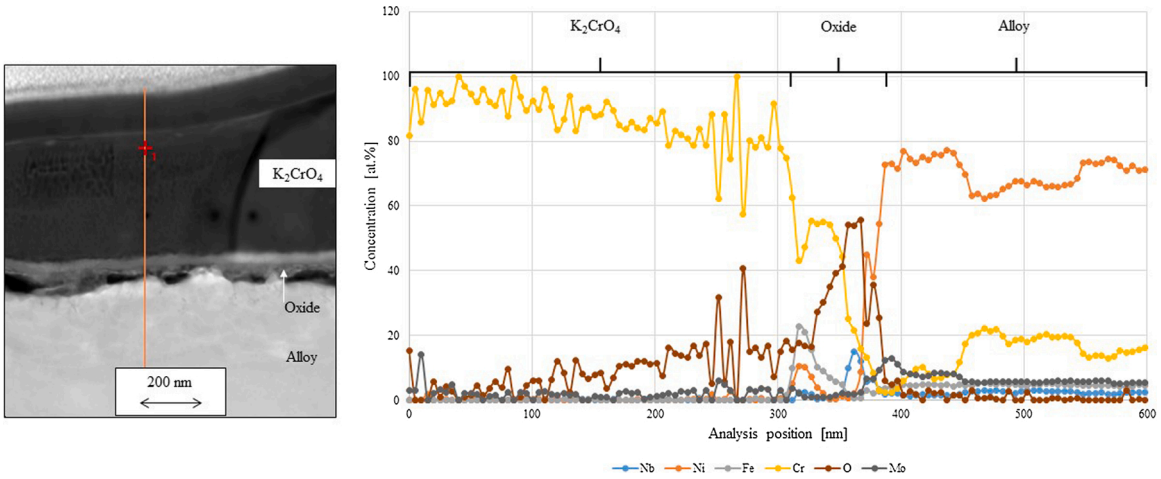

Fig. 11. An EDX line scan through a K_2CrO_4 particle and the thin oxide scale formed on the Alloy 625 sample. The red cross marks the starting point of the line scan. (For interpretation of the references to colour in this figure legend, the reader is referred to the web version of this article.)

chromium oxide inner layer. A chromium-depleted region was identified below the oxide, evidencing chromium diffusion from the alloy into the oxide (Fig. 7). A few separate voids were visible in the chromium-depleted region. These are most likely coalesced vacancies in the reaction layer, known as Kirkendall voids [30]. The presence of the oxide scale below the inclusion indicates that the detachment of the inclusion originated from the rapid oxidation of the rare-earth elements and/or from the thermal expansion coefficient mismatch of the formed oxides. After the detachment, further oxidation of the exposed alloy took place. Based on this, easily oxidizing inclusions right beneath the alloy surface might function as pathways for reactive process gasses to ingress the material, resulting in enhanced local failure.

In the presence of a KCl pellet, an oxide scale with a thickness between 60 and 400 nm formed on the Sanicro 28 alloy (Fig. 8). In addition

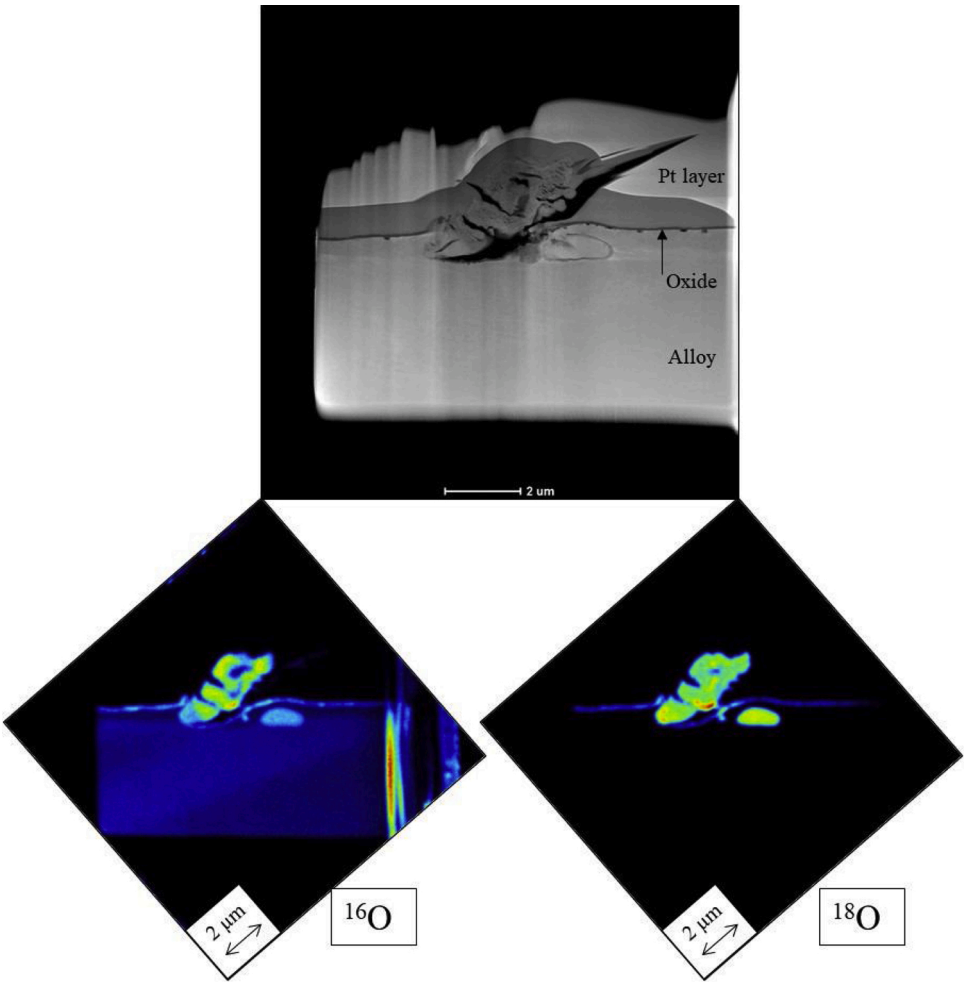

Fig. 12. Nano-SIMS maps for oxygen isotopes measured on the reference Sanicro 28 sample located on the windward side of KCl.

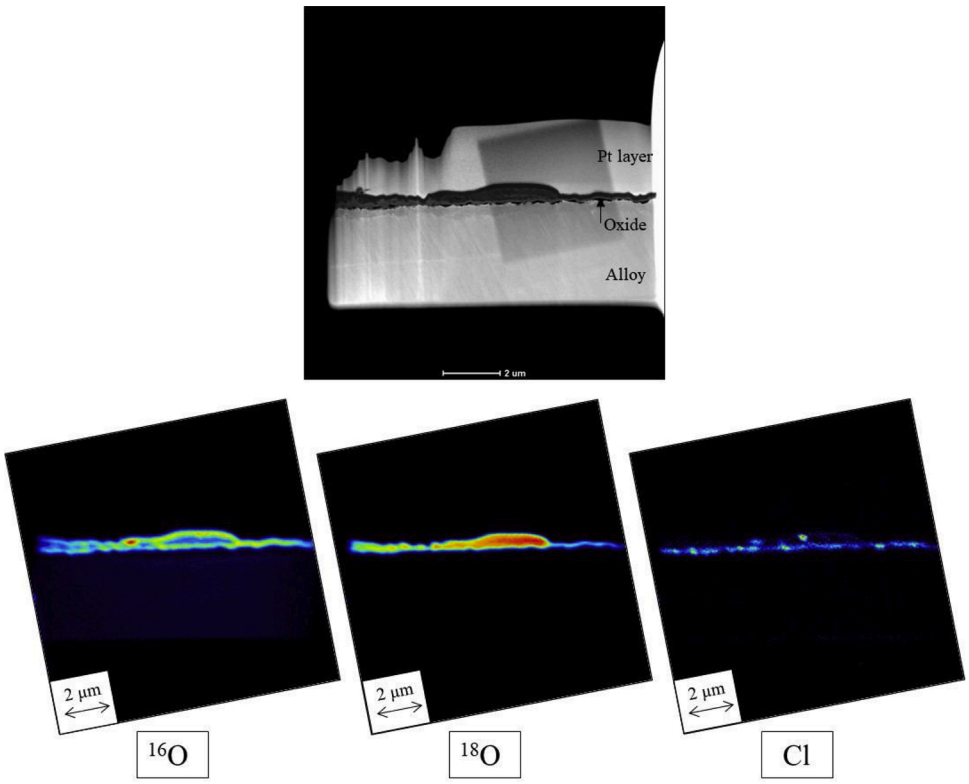

Fig. 13. Nano-SIMS maps for negative ions measured on the Sanicro 28 sample with a KCl pellet.

to the greater oxide thickness variation compared to the reference sample, K_2CrO_4 is clearly observable on top of the oxide. The scale consisted of an outermost iron oxide layer, followed by a mixed oxide containing Fe, Mn, and Cr before a chromia layer (Fig. 9). Austenitic alloys with more than 17 % chromium are known to form a double-layered oxide scale with an outer layer of $(Mn,Fe)Cr_2O_4$ spinel and an inner layer of pure chromia [31]. The identified iron oxide layer formed as a result of chromium diffusion into K_2CrO_4 particles and due to the high enough oxygen partial pressure, stabilizing iron oxide and allowing it to grow more rapidly than $(Mn,Fe)Cr_2O_4$ and Cr_2O_3. Manganese diffuses to the alloy surface along grain boundaries and dislocations, so the fact that a Mn-containing spinel forms in the presence of KCl suggests that KCl affects the oxidation kinetics and the oxide structure either through chromium depletion and/or by increasing the number of suitable diffusion pathways. As with the reference sample, a Cr-depleted zone was identified underneath the oxide scale, in the bulk material. Furthermore, the number and size of the Kirkendall voids were larger than in the reference sample.

Alloy 625 oxidized slower than Sanicro 28 in the presence of KCl, forming an oxide scale with a thickness of around 60 nm (Fig. 10). The oxide is comprised of several superimposed layers, starting with an iron/nickel oxide as the outermost layer, followed by a chromia layer with niobium enrichment at the oxide/alloy interface (Fig. 11). As with Sanicro 28, a chromium-depleted region is identified from beneath the oxide scale. A typical protective oxide of Alloy 625 consists almost solely of Cr_2O_3, possibly with smaller amounts of NiO, Nb_2O_3, and $NbCrO_4$ [32]. The growth of an iron-containing oxide scale, despite the low iron content of the alloy and relatively short exposure time used in the present study, indicates a rapid initiation of corrosion, induced by KCl. The cause for the observed iron-containing oxide formation is chromium depletion through chromate formation. Over longer exposure times, niobium oxidation may provide additional pathways for aggressive species to ingress into the material [33].

3.2.2. Nano-SIMS

The very thin surface oxide formed on the Sanicro 28 reference sample contained both oxygen isotopes (Fig. 12). The oxidized cerium inclusion contained both oxygen isotopes, but the isotopes were not evenly distributed. Interestingly, another Ce inclusion below the surface oxide was also oxidized, but it contained mainly the ^{18}O isotope. This supports a previous finding, where the oxide particles of yttrium, another reactive element, acted as a gateway for water to access the interface between the oxide and the alloy [34]. However, a reaction with water only occurs, when the reactive element particle is oxidizing during the exposure. Applied reactive element oxide coatings are reported to reduce alloy oxidation remarkably [35]. The presence of both oxygen isotopes inside the oxidized cerium inclusion originates most likely from the rapid oxidation of cerium, during which the oxidizing metal utilizes whatever oxygen is available.

The surface oxide of the Sanicro 28 sample with a KCl pellet contained both oxygen isotopes, but the ^{18}O isotope was enriched in the outermost layers of the oxide (Fig. 13). In the case of the chromate particle, its core contained solely ^{18}O isotope, surrounded by a ^{16}O-rich crust. Earlier, when metal samples have been exposed simultaneously to $^{16}O_2$ and $H_2^{18}O$, both oxygen isotopes have been identified in the formed oxide, but a larger part originated from water vapor [36,37]. The enhanced oxidation in the presence of water vapor stems from the easier dissociation of water compared to molecular oxygen. The dissociation of water releases interstitial protons, which lower the vacancy formation energy, enhance vacancy clustering, and increase ion diffusion [38]. The initial ingress of water molecules through the surface oxide has been proposed to take place via hydrolysis, where [M-O-M] + H_2O ↔ [M-OH…HO-M] transformations enable the self-diffusion of water as formally neutral entities [39]. Chlorine was found beneath the surface oxide, most likely as solid metal chlorides ($CrCl_3$ and $FeCl_2$) [40]. The surface oxide was dense enough to maintain a low oxygen partial pressure beneath the oxide scale, making the metal chlorides stable. Gaseous chromium chloride converts into chromium oxide at lower oxygen partial pressure than gaseous iron chloride. Because of this,

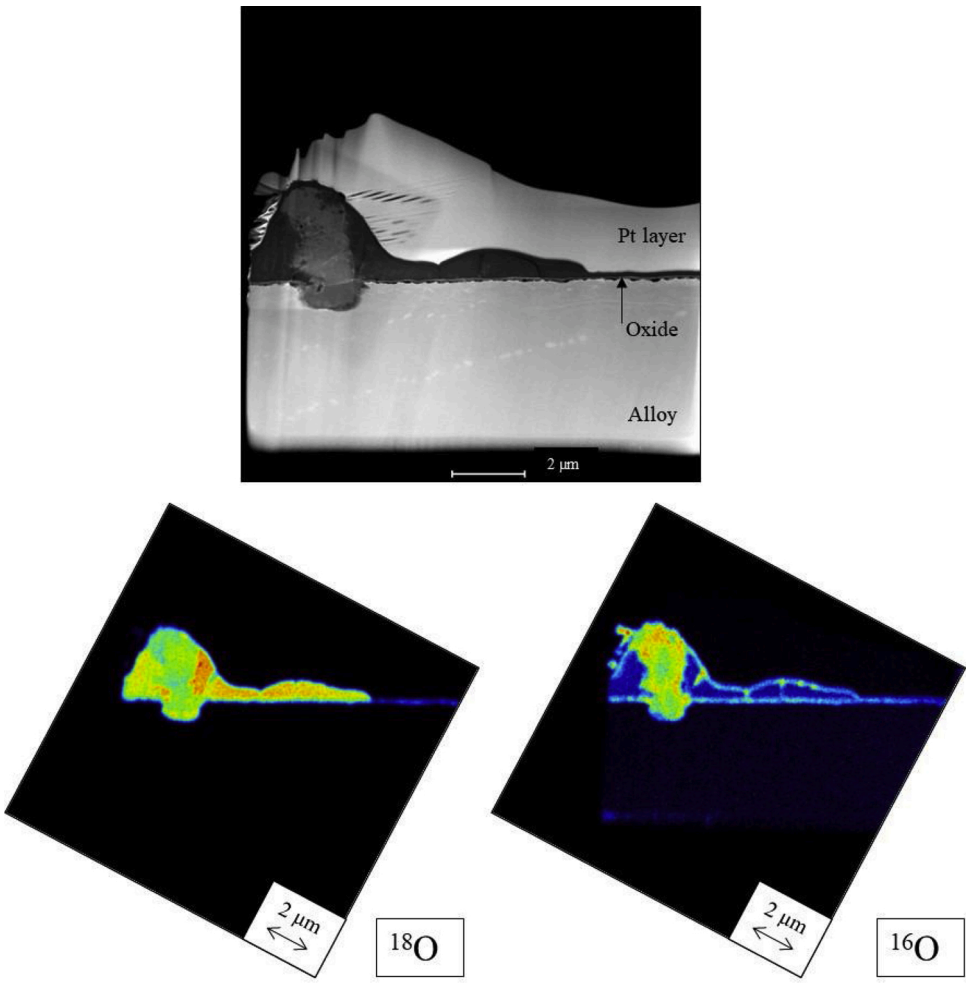

Fig. 14. Nano-SIMS maps for oxygen isotopes measured on the Alloy 625 sample.

chromium oxide forms closer to the alloy surface. This agrees well with the results from the STEM line scans, where an iron-rich outer oxide layer and a chromium-rich inner oxide layer were identified.

The surface oxide of the Ni-based Alloy 625 contains both oxygen isotopes with the ^{18}O isotope enriched in the outermost layer of the oxide, followed by a thin inner layer containing the ^{16}O isotope (Fig. 14). In the case of the chromate particles, the core contained solely ^{18}O isotope, surrounded by a ^{16}O-rich crust. The oxygen isotope distribution was similar to the one identified in Sanicro 28 and occurred most likely by the reasons described in the text above. Similar to the oxidation of cerium, the oxidized Nb particle in Alloy 625 contained both oxygen isotopes. The rapid oxidation of niobium was most likely the cause for both oxygen isotopes being present in the formed niobium oxide. One characteristic of the niobium reaction is the large volumetric expansion of niobium oxidation, generating micro-cracks, which may act as short circuit pathways for reactive species [33]. Chlorine was not detected underneath the oxide. Nickel-based alloys withstand in general high-temperature corrosion better than iron-based alloys, so the oxide scale on Alloy 625 was most likely so thin that the oxygen partial pressure was not low enough to stabilize any metal chlorides. Instead, they oxidized and released the chlorine to exit the furnace as HCl with the gas flow.

4. Conclusions

The role of two oxygen sources, oxygen and water vapor, in the initiation of KCl-induced high-temperature corrosion was addressed by studying two high-alloyed commercial materials at 550 °C. The differentiation between the two oxygen sources was implemented by using ^{18}O-enriched water and $^{16}O_2$. After the exposures, the isotopes were identified with surface ToF-SIMS and cross-sectional nano-SIMS. The surface morphologies were imaged with SEM and the surface compositions were determined by EDX and XPS. Further oxide characterization was carried out with cross-sectional STEM/EDX analyses.

Both alloys reacted with KCl by forming solid potassium chromate (K_2CrO_4) on the alloy surface. Over time, the chromate formation depletes the protective surface oxide in chromium and the alloys then become susceptible to further attack. The amount of the formed K_2CrO_4 decreased as a function of lateral distance from the KCl pellet present on the surface, suggesting that the solid-solid reaction between KCl(s) and the protective oxide appeared to be more responsible for chromium depletion than the gas-solid reaction between KCl(g) and the protective oxide. In addition to chromate formation, cerium and niobium were rapidly oxidized in the vicinity of the alloy surfaces, providing short-circuit pathways for reactive species into the bulk material. The nano-SIMS analyses revealed water to be more involved in the above-mentioned reactions than O_2: ^{18}O was the main oxygen isotope found in the surface oxides and K_2CrO_4 particles. The higher reactivity of water is presumed to originate from water dissociation and hydrolysis resulting in enhanced vacancy clustering and increased ion diffusion. The results provide further evidence on the active role of water vapor in salt-induced high-temperature corrosion reactions taking place in various industrial processes.

Data availability

The raw/processed data required to reproduce these findings cannot be shared at this time due to technical or time limitations.

CRediT authorship contribution statement

Juho Lehmusto: Conceptualization, Methodology, Resources, Investigation, Visualization, Formal analysis, Writing - original draft. **Mohammad Sattari:** Conceptualization, Methodology, Resources, Investigation, Formal analysis, Writing - review & editing. **Mats Halvarsson:** Conceptualization, Writing - review & editing, Supervision. **Leena Hupa:** Conceptualization, Writing - review & editing, Supervision.

Declaration of Competing Interest

The authors declare that they have no known competing financial interests or personal relationships that could have appeared to influence the work reported in this paper.

Acknowledgments

This work has been carried out within the Academy of Finland project “Novel Approaches to Study Corrosion Mechanisms in High-temperature Industrial Processes” (Decision no. 296435). The authors are very grateful to Mr. Aurélien Thomen for the NanoSIMS measurements, which were obtained at the Chemical Imaging Infrastructure, Chalmers University of Technology and University of Gothenburg, which is supported by the Knut and Alice Wallenberg Foundation.

References

[1] M. Broström, H. Kassman, A. Helgesson, M. Berg, C. Andersson, R. Backman, A. Nordin, Sulfation of corrosive alkali chlorides by ammonium sulfate in a biomass fired CFB boiler, Fuel Process. Technol. 88 (11–12) (2007) 1171–1177.
[2] J.N. Knudsen, P.A. Jensen, K. Dam-Johansen, Transformation and release to the gas phase of Cl, K, and S during combustion of annual biomass, Energy & Fuels 18 (5) (2004) 1385–1399.
[3] N. Orang, H. Tran, Effect of feedstock moisture content on biomass boiler operation, TAPPI J. 14 (10) (2015) 629–637.
[4] J. Lehmusto, P. Yrjas, B.-J. Skrifvars, M. Hupa, High temperature corrosion of superheater steel by KCl and K_2CO_3 under dry and wet conditions, Fuel Process. Technol. 104 (2012) 253–264.
[5] S. Kiamehr, K.V. Dahl, M. Montgomery, M.A.J. Somers, KCl-induced high temperature corrosion of selected commercial alloys. Part 1: chromia-formers, Mater. Corros. 66 (12) (2015) 1414–1429.
[6] S.C. Okoro, M. Montgomery, F.J. Frandsen, K. Pantleon, Effect of water vapor on high-temperature corrosion under conditions mimicking biomass firing, Energy & Fuels 29 (9) (2015) 5802–5815.
[7] M. Montgomery, A. Karlsson, O.H. Larsen, Field test corrosion experiments in Denmark with biomass fuels. Part 1: straw-firing, Mater. Corros. 53 (2) (2002) 121–131.
[8] L.A. Hansen, H.P. Nielsen, F.J. Frandsen, K. Dam-Johansen, S. Hørlyck, A. Karlsson, Influence of deposit formation on corrosion at a straw-fired boiler, Fuel Process. Technol. 64 (1–3) (2000) 189–209.
[9] P. Viklund, A. Hjörnhede, P. Henderson, A. Stålenheim, R. Pettersson, Corrosion of superheater materials in a waste-to-energy plant, Fuel Process. Technol. 105 (2013) 106–112.
[10] J. Pettersson, H. Asteman, J.-E. Svensson, L.-G. Johansson, KCl induced corrosion of a 304-type austenitic stainless steel at 600°C; the role of potassium, Oxid. Met. 64 (1–2) (2005) 23–41.
[11] W.J. Quadakkers, A. Elschner, W. Speier, H. Nickel, Composition and growth mechanisms of alumina scales on FeCrAl-based alloys determined by SNMS, Appl. Surf. Sci. 52 (4) (1991) 271–287.
[12] R. Prescott, M.J. Graham, The formation of aluminum oxide scales on high-temperature alloys, Oxid. Met. 38 (3–4) (1992) 233–254.
[13] T. Horita, K. Yamaji, T. Kato, N. Sakai, H. Yokokawa, Imaging of labeled gas movements at the SOFC electrode/electrolyte interfaces, Solid State Ionics 169 (1-4) (2004) 105–113.
[14] J.A. Costello, R.E. Tressler, Isotope labeling studies of the oxidation of silicon at 1000° and 1300 °C, J. Electrochem. Soc. 131 (8) (1984) 1944–1947.
[15] U.S. Ozkan, S.A. Driscoll, L. Zhang, K.L. Ault, Investigation of oxygen insertion mechanism in selective oxidation reactions over $MnMoO_4/MoO_3$ catalysts through isotopic labeling and chemisorption studies, J. Catal. 124 (1) (1990) 183–193.
[16] M. Michalik, M. Hänsel, W.J. Quadakkers, Effect of Water Vapour on Growth and Adherence of Chromia Scales on Pure Chromium, Report Forschungszentrum Jülich, 67, 2007.
[17] J. Zurek, D.J. Young, E. Essuman, M. Hänsel, H.J. Penkalla, L. Niewolak, W. J. Quadakkers, Growth and adherence of chromia based surface scales on Ni-base alloys in high- and low-pO_2 gases, Mater. Sci. Eng. A 477 (1–2) (2008) 259–270.
[18] H. Falk-Windisch, P. Malmberg, M. Sattari, J.-E. Svensson, J. Froitzheim, Determination of the oxide scale growth mechanism using ^{18}O-tracer experiments in combination with transmission electron microscopy and nanoscale secondary ion mass spectrometry, Mater. Charact. 136 (2018) 128–133.
[19] J. Lehmusto, M. Bergelin, J. Sui, J. Juhanoja, B.-J. Skrifvars, P. Yrjas, Applicability of ToF-SIMS and stable oxygen isotopes in KCl-induced corrosion studies at high temperatures, Corros. Sci. 125 (2017) 1–11.
[20] V.B. Trindade, U. Krupp, Ph.E.-G. Wagenhuber, H.-J. Christ, Oxidation mechanisms of Cr-containing steels and Ni-base alloys at high-temperatures – part I: the different role of alloy grain boundaries, Mater. Corros. 56 (11) (2005) 785–790.
[21] J. Lehmusto, D. Lindberg, P. Yrjas, L. Hupa, The effect of temperature on the formation of oxide scales regarding commercial superheater steels, Oxid. Met. 89 (2018) 251–278.
[22] T.N. Rhys-Jones, H.J. Grabke, H. Kudielka, The effects of various amounts of alloyed cerium and cerium oxide on the high temperature oxidation of Fe-10Cr and Fe-20Cr alloys, Corros. Sci. 27 (1) (1987) 49–73.
[23] T. Sorvajärvi, A. Manninen, J. Toivonen, J. Saarela, R. Hernberg, Resonant photoacoustic cell for pulsed laser analysis of gases at high temperature, Rev. Sci. Instrum. 80 (2009), 123103.
[24] J. Sui, J. Lehmusto, M. Bergelin, M. Hupa, The onset of potassium chloride induced high temperature corrosion: a novel experimental approach, Oxid. Met. 82 (2014) 437–456.
[25] R. Steinberger, J. Duchoslav, T. Greunz, M. Arndt, D. Stifter, Investigation of the chemical stability of different Cr(VI) based compounds during regular X-ray photoelectron spectroscopy measurements, Corros. Sci. 90 (2015) 562–571.
[26] P.P. Pansila, N. Witit-anun, S. Chaiyakun, Effect of oxygen partial pressure on the morphological properties and the photocatalytic activities of titania thin films on unheated substrates by sputtering deposition method, Adv. Mater. Res. 770 (2013) 18–21.
[27] J. Hou, A.H. Liu, M. Liu, B.Y. Man, J.J. Guo, D.M. Kong, Effect of oxygen partial pressure on morphology of ZnO nanostructure prepared on Zn films by simple evaporation without any additive, Mater. Res. Innov. 16 (4) (2012) 271–275.
[28] S.R.J. Saunders, M. Monteiro, F. Rizzo, The oxidation behaviour of metals and alloys at high temperatures in atmospheres containing water vapour: a review, Prog. Mater Sci. 53 (5) (2008) 775–837.
[29] G.M. Raynaud, R.A. Rapp, In situ observation of whiskers, pyramids and pits during the high-temperature oxidation of metals, Oxid. Met. 21 (1–2) (1984) 89–102.
[30] A.D. Smigelskas, E.O. Kirkendall, Zinc diffusion in alpha brass, Am. Inst. Min. Metall. Eng. 13 (7) (1946) 1–5.
[31] C. Ostwald, H.J. Grabke, Initial oxidation and chromium diffusion. I. Effects of surface working on 9–20% Cr steels, Corros. Sci. 46 (5) (2004) 1113–1127.
[32] C. Cuevas-Arteaga, D. Verhelst, A. Alfantazi, Performance of alloy 625 under combustion gas environments – a review, ECS Trans. 28 (24) (2010) 61–76.
[33] H. Chen, H. Wang, Q. Sun, C. Long, T. Wie, S.H. Kim, J. Chen, C. Kim, C. Jang, Oxidation behavior of Fe-20Cr-25Ni-Nb austenitic stainless steel in high-temperature environment with small amount of water vapor, Corros. Sci. 145 (2018) 90–99.
[34] N. Mortazavi, C. Geers, M. Esmaily, V. Babic, M. Sattari, K. Lindgren, P. Malmberg, B. Jönsson, M. Halvarsson, J.-E. Svensson, I. Panas, L.-G. Johansson, Interplay of water and reactive elements in oxidation of alumina-forming alloys, Nat. Mater. 17 (7) (2018) 610–617.
[35] R.J. Hussey, M.J. Graham, The influence of reactive-element coatings on the high-temperature oxidation of pure-Cr and high-Cr-content alloys, Oxid. Met. 45 (3–4) (1996) 349–374.
[36] G. Hultquist, L. Gråsjö, Q. Lu, T. Åkermark, The analysis of gas consumption in the reaction of Fe and Cu in $H_2^{16}O/H_2^{18}O/O_2$ gas mixtures, Corros. Sci. 36 (9) (1994) 1459–1471.
[37] M. Göbel, J.D. Sunderkötter, D.I. Mircea, H. Jenett, M.F. Stroosnijder, Study of the high-temperature oxidation behaviour of Ti and Ti4Nb with SNMS using tracers, Surf. Interface Anal. 29 (5) (2000) 321–324.
[38] L. Luo, M. Su, P. Yan, L. Zou, D.K. Schreiber, D.R. Baer, Z. Zhu, G. Zhou, Y. Wang, S.M. Bruemmer, Z. Xu, C. Wang, Atomic origins of water-vapour-promoted alloy oxidation, Nat. Mater. 17 (2018) 514–518.
[39] J.R.T. Johnson, I. Panas, Hydrolysis on transition metal oxide clusters and the stabilities of M-O-M bridges, Inorg. Chem. 39 (15) (2000) 3192–3204.
[40] A. Zahs, M. Spiegel, H.J. Grabke, Chloridation and oxidation of iron, chromium, nickel and their alloys in chloridizing and oxidizing atmospheres at 400-700 °C, Corros. Sci. 42 (6) (2000) 1093–1122.